Determination of Critical Gas Saturation by Micro-CT

Steffen Berg[1,3], *Ying* Gao[1,3], *Apostolos* Georgiadis[1,3], *Niels* Brussee[1], *Ab* Coorn[1], *Hilbert* van der Linde[1], *Jesse* Dietderich[2], *Faruk Omer* Alpak[2], *Daniel* Eriksen[1], *Miranda* Mooijer-van den Heuvel[1], *Jeff* Southwick[1], *Matthias* Appel[1], *Ove Bjørn* Wilson[1]

[1]Shell Global Solutions International B.V., Grasweg 31, 1031 KC Amsterdam, The Netherlands
[2]Shell International Exploration and Production Inc., 3333 Highway 6 South, Houston, TX 77210, USA
[3]Department of Earth Science & Engineering, Imperial College London, Kensington SW7 2AZ, UK

Abstract. The critical gas saturation was directly determined using micro-CT flow experiments and associated image analysis. The critical gas saturation is the minimum saturation above which gas becomes mobile and can be produced. Knowing this parameter is particularly important for the production of an oil field that during its lifetime falls below the bubble point which will reduce the oil production dramatically. Experiments to determine the critical gas saturation are notoriously difficult to conduct with conventional core flooding experiments at the Darcy scale. The difficulties are primarily related to two effects: The development of gas bubbles is a nucleation process which is governed by growth kinetics that, in turn, is related to the extent of pressure drawdown below the bubble point. At the Darcy scale, the critical gas saturation at which the formed gas bubbles connect to a percolating path, is typically probed via a flow experiment, during which a pressure gradient is applied. This leads not only to different nucleation conditions along the core but also gives no direct access to the size and growth rate of gas bubbles before the percolation. In combination, these two effects imply that the critical gas saturation observed in such experiments is dependent on permeability and flow rate, and that the critical gas saturation relevant for the (equilibrium) reservoir conditions has to be estimated by an extrapolation. Modern Digital Rock related experimentation and modelling provides a more elegant way to determine the critical gas saturation. We report pressure depletion experiments in mini-cores imaged by X-ray computed micro-tomography (micro-CT) that allowed the direct determination of the connectivity of the gas phase. As such, these experiments enabled the detection of the critical gas saturation via the percolation threshold of the gas bubbles. Furthermore, the associated gas- and oil relative permeabilities can be obtained from single-phase flow simulations of the connected pathway fraction of gas and oil, respectively.

INTRODUCTION

The critical gas saturation is the saturation at which the gas that comes out of solution below the bubble point of a hydrocarbon mixture becomes mobile inside of porous rock ("critical gas"). This is relevant for the production of oil fields that during their lifetime fall below the bubble point which will reduce the oil production dramatically. The critical gas saturation is also an important parameter for correct dynamic modelling. Experimentally observed critical gas saturations range between 0.5-50% depending on fluid and rock properties, pressure decline rate and experimental protocols [1,2]. Such experiments are notoriously difficult to conduct [3-6]. The development of gas bubbles is a nucleation process at a growth rate related to pressure drawdown below the bubble point and associated supersaturation [3,8-12]. When operating at a constant pressure decline rate there is an interplay between supersaturation of the liquid, the rate of gas bubble nucleation [5,18], growth kinetics [3] and the rate of pressure decline [1]. Thus critical gas saturations observed under experimentally achievable decline rates ranging from 10-50% [1-6] are extrapolated to the pressure decline rate in the field resulting in critical gas saturations in the range of typically 3-15% [1,2,8-12]. The wide range of observed critical gas saturations occurs not only because of differences in decline rate but also because of different regimes [3]. For pressure depletion mode without any significant flow reflecting a nucleation process one would expect a critical gas saturations in the same range as a residual gas saturation, i.e. above 20-30% [16,17] which is consistent with typical percolation thresholds in 3D between 20-32% [21-25]. Experiments where the saturation at which gas becomes mobile is probed by a flow measurement observe typically much lower critical gas saturations. Due to the low viscosity the gas phase is significantly more mobile than a liquid which can cause viscous fingering at the pore scale [27] and lead to a connected pathway significantly below percolation thresholds. Viscous fingering may be significantly enhanced at near-miscible conditions where interfacial tension is very low [28,29]. In the field flow and gas

* Corresponding author: steffen.berg@shell.com

expansion processes can be coupled e.g. in solution gas drive [19,20]. The critical gas saturation depends on exactly how depletion and flow are coupled which can vary from field to field and by the distance from the well-bore. The experimentally observed critical gas saturation therefore depends on the respective experimental protocol and the associated pore scale fluid distribution [17].

Most Darcy scale experiments involve substantial instrumental complexity and efforts while the results are still impacted by protocols and interpretation methodology [6,7]. Saturation monitoring by X-ray [6,7,18] has improved the interpretation. For instance, in low-permeability rock the (significant) pressure gradient crosses the bubble point in the rock at a location that can be determined via saturation monitoring by X-ray [6] allowing to infer the critical gas saturation. Still one of the main shortcomings of Darcy-scale experiments is that the critical gas saturation is inferred from either flow or saturation (gradients). It is difficult to clearly separate the regimes of quasi-static nucleation and unstable flow. Using micro-CT imaging allows to determine directly the connectivity of the gas phase inside the pores at the point of critical gas (phase fraction) where non-percolating gas bubbles can be already observed above the bubble point and the critical gas saturation is detectable via the percolation threshold. This study provides a proof-of-concept where methodology and workflow are assessed. Two central questions are addressed: (1) is the natural contrast between gas and liquid large enough to segment gas and liquid without any contrast agent and (2) can pressure and gas nucleation controlled precisely enough in a small rock sample suitable for µCT such that the percolation threshold i.e. the critical gas saturation can be determined.

METHODS AND MATERIALS

The experimental methodology is based on imaging the gas distribution directly inside the pore space by X-ray computed micro-tomography. A Bentheimer sandstone sample (porosity = 19.1%, permeability = 2500 mD, 4 mm diameter and 20 mm length) is enclosed in a rubber sleeve and mounted into a custom-built core holder shown in **Figure 1** which is made from PEEK which can operate to a pressure of 30 bar and a temperature of 60 °C. Note that this setup is meant for a proof-of-concept and the operating envelope of this experiment can be extended to higher pressures and temperature to correspond to reservoir conditions. A mixture of n-decane and n-propane was chosen as gas-liquid model system that has an extended two-phase region within the operating envelope of the setup. The phase behaviour including the liquid-vapour split is displayed in **Figure 2**. The phase split has been computed with Shell's proprietary STFlash tool using the Shell modified Redlich-Kwong (SMIRK) equation of state (EOS) [26]. Based on the flash calculations a 50% molar fraction of propane was chosen, for ambient temperature (22°C in the laboratory and pumps, and 27°C inside the µCT). The EOS calculated bubble point pressure for that experimental condition is 4.77 bar at an interfacial tension of 17 mN/m (at 4.69 bar, using a parachor approach). Given the experimental uncertainties on mixing and thermal equilibration we would expect a bubble point between 2 and 5 bar.

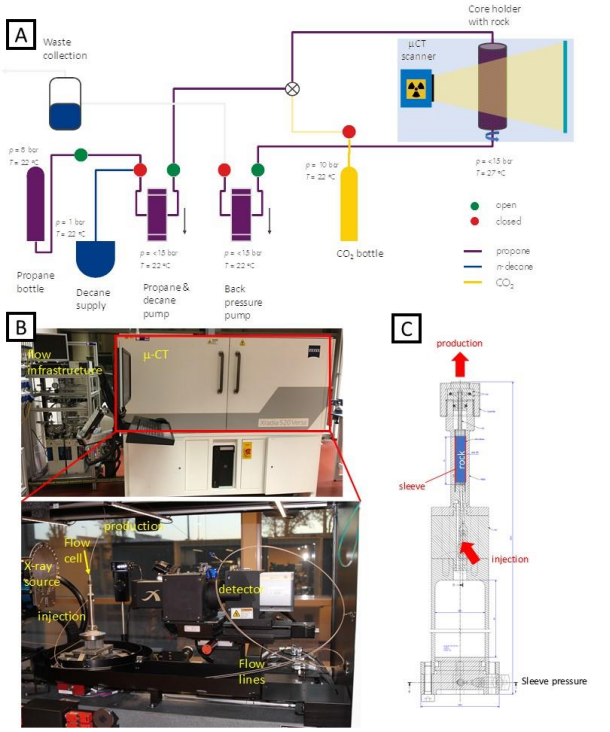

Figure 1. Schematic overview of the experimental setup (A) consisting of the flow infrastructure and the micro-CT scanner (B) and the core holder with the rock sample (C). Injection occurs from bottom to top.

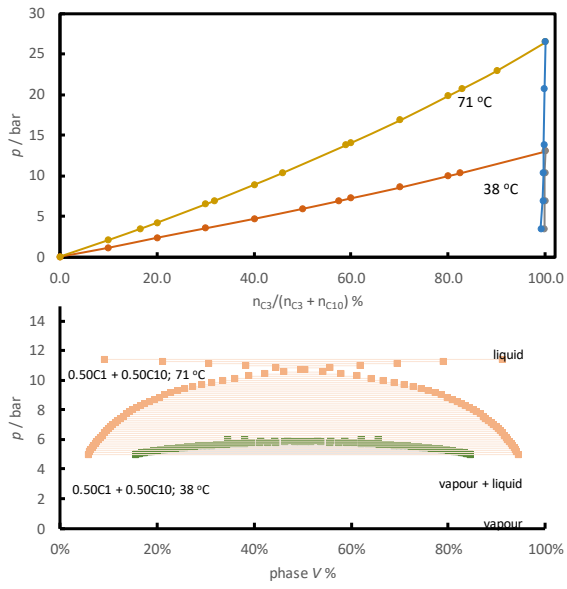

Figure 2. Phase envelopes of the propane-decane mixture for different temperatures as a function of composition (top) and liquid-vapor phase split (bottom).

Micro-CT imaging has been conducted with a Zeiss Versa 520 micro-CT scanner at 0.4x magnification at 80 kV and a power of 7W. A 2x2 binning of the detector was used at an exposure time of 1.3 s. 1401 projections have been used for reconstruction, leading to an overall scan time of

about 1 hour. This protocol was determined by systematic variation of resolution, number of projections and integration time in order to arrive at a reconstructed image where the gas can be segmented. µCT scans were always taken at pressure equilibrium conditions. During post-processing, no indications of fluid moment during the scanning time was observed. For image processing (Avizo 9, ThermoFisher) all images are registered on the dry scan. Then a cylinder is cropped to remove the rubber sleeve encapsulating the sample within the confining pressure. A non-local means filter [34] (search window: 21px; local neighbourhood: 4 px; similarity value: 3) is applied twice to remove image noise. Each scan is then segmented by the watershed region growing method.

RESULTS

The first set of experiments has been conducted in either pressurization or pressure depletion modes of the pore fluids in absence of any external flow. In experiments where the pressure was lowered in small (0.1 bar) increments with significant equilibration time at each step, the observed bubble point was typically below 2 bar, and once reached, a significant amount of gas came out of solution leading to instantaneous percolation from top to bottom. This is consistent with the observation of a bubble point depression [3] which basically prevents us from probing the percolation threshold in a very gradual way.
In the following we present two strategies to overcome this observation challenge. In both cases, the pressure is initially drawn significantly below the bubble point to initiate bubble nucleation. In the first mode, the *pressurization mode*, the pore pressure has been initially drawn down such that a significant fraction of gas came out of solution and became immediately connected. Subsequently, the pore pressure was increased in steps to gradually reduce the size of gas bubbles and eventually reach the percolation threshold for the gas phase. The second mode, *the pressure depletion mode*, aims at nucleating bubbles rapidly but then bringing the pressure quickly back to the expected bubble point in order to prevent the formation of large percolating gas bubbles. The percolation threshold is then reached upon further pressure depletion.

Pressurization mode

Experiment 1 was conducted in pressurization mode. The pore pressure as a function of time is shown in **Figure 3** which also shows the micro-CT scan intervals. The dry scan was taken before start of the experiment. A fully liquid-saturated scan was taken right before the start of the pressure depletion which is the first scan interval shown in **Figure 3**. After the initial pressure drawdown, a significant amount of gas is nucleated which – as we will see later - percolates across the whole pore space. In **Figure 4**, pressure vs. volume for Experiment 1 is displayed. On can clearly see the initial fluid compressibility effect and the suppressed nucleation similar to what is reported in the literature [3]. Upon further drawdown the gas is nucleated and then compressed during pressurization. Extrapolating the liquid-gas p-V line during the re-pressurization to the intersect with the liquid p-V line during initial pressure depletion gives an indication of the bubble-point, which is consistent with experimental observation of bubble points around 3 bar. The area under the liquid-gas line would be characterized by the supersaturation and nucleation regime where the system is not in a phase equilibrium [3].

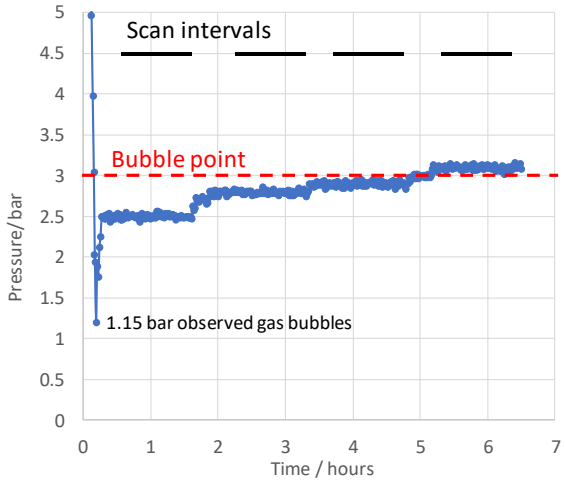

Figure 3. Pressure during experiment 1. The initial pressure drawdown below the bubble point causes a large amount of gas coming out of solution which percolates through the whole pore space. The gas is compressed and dissolves in the liquid until it is not connected anymore. The intervals where micro-CT scans were taken are indicates by black lines.

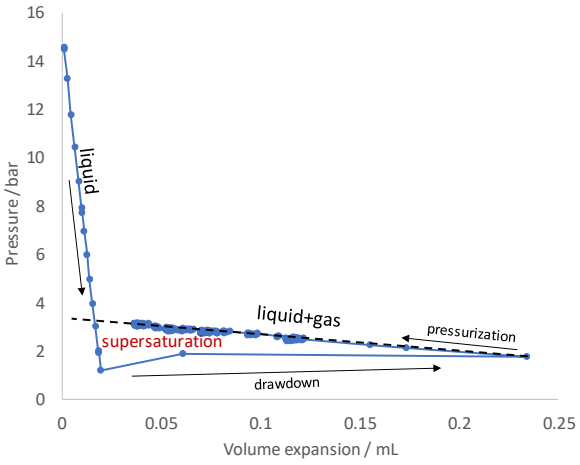

Figure 4. Pressure vs. volume for experiment 1 which was conducted in pressurization mode. The initial pressure depletion leads to a supersaturation without nucleation of gas [3]. The percolation threshold is reached upon pressurization.

The 3D images of the experiment shown in **Figure 5** are consistent with the pressure-volume signature from **Figure 3** and **Figure 4**. The initial depletion and equilibration lead to a large volume of gas coming out of solution which percolates from inlet to outlet. Most of the clusters are connected. In **Figure 5** a cluster analysis was performed, and each gas cluster is labelled and displayed in a different colour. The scan displayed in **Figure 5A**

represents the first equilibration step after pressure drawdown. The gas phase forms one large cluster which percolates through the whole pore space. Upon pressurization the gas saturation decreases, gas clusters shrink and lose more and more their connectivity as shown in **Figure 5 B-D** (more colours appear indicating more disconnected clusters).

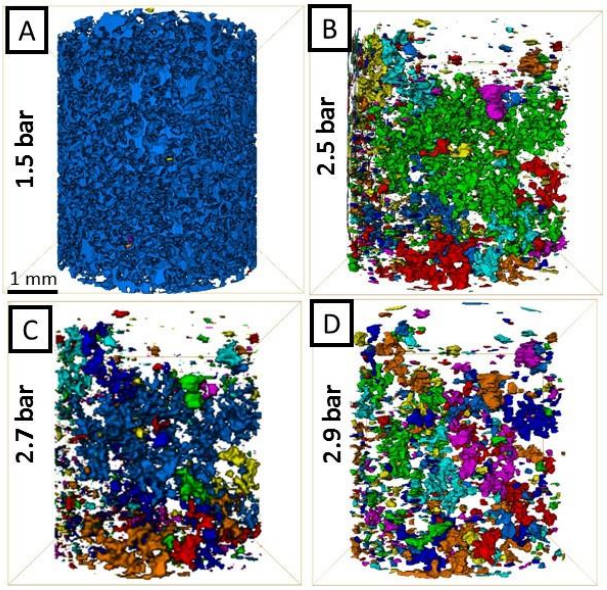

Figure 5. Micro-CT images taken during experiment 1. Each connected gas cluster is shown in a different colour. After the initial pressure drawdown to 1.5 bar almost the whole pore space is filled by gas, which is almost entirely connected (A). Upon pressurization the gas saturation decreases, and gas clusters shrink losing more and more their connectivity (B-C) until at 2.9 bar the top-bottom connectivity is finally lost (D).

Pressure depletion mode

Experiment 2 is conducted in pressure depletion mode. In order to nucleate small, non-percolating gas bubbles, the pressure is initially drawn down to 1.6 bar and then quickly raised again to 3.0 bar which is approximately the bubble point as shown in **Figure 6**.

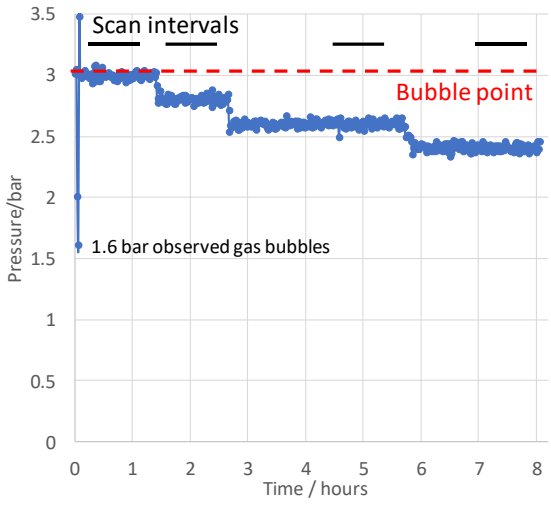

Figure 6. Pressure during experiment 1. The initial pressure drawdown below the bubble point causes a large amount of gas coming out of solution which percolates through the whole pore space. The gas is increasingly compressed until it is not connected anymore.

In **Figure 7.** pressure vs. volume for Experiment 1 is displayed. After initial depressurization and fluid compressibility effects, gas is nucleated by a brief pressure drawdown and immediate re-pressurization followed by pressure depletion. The regime where phase equilibrium is still visible but less pronounced than in experiment 1 (**Figure 4**). This is apparently an effect of the quick drawdown and respective rapid bubble nucleation. Overall the applied protocol is indeed successful.

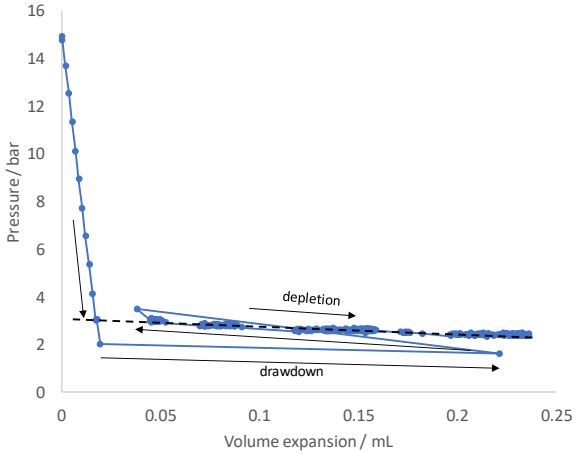

Figure 7. Pressure vs. volume for experiment 2 which was conducted in pressure depletion mode. Due to the very quick drawdown the supersaturated regime where nucleation of bubbles is suppressed and there is no phase equilibrium is avoided to a large extent.

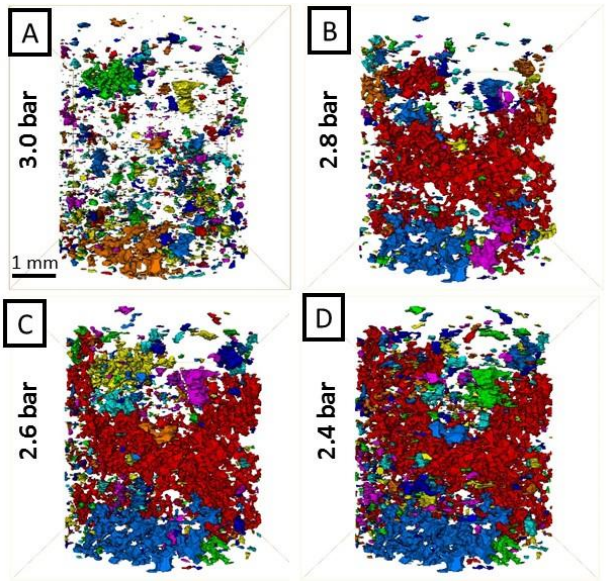

Figure 8. Micro-CT images taken during experiment 2. After the very quick initial pressure drawdown during which small gas bubbles are nucleated, the pore pressure is raised again to 3.0 bar leaving a set of small, not-connected gas bubbles (A). Upon pressure depletion, the gas saturation increases, and gas clusters grow increasing their connectivity (B-D).

The successful experimental protocol is also supported by the 3D images displayed in **Figure 8**. **Figure 8A** was taken right after pressure drawdown and re-equilibration

at the expected bubble point. Small, not-connected gas bubbles were observed. Upon closer inspection of **Figure 7.** we observe that the one data point at 1.6 bar is associated with a volume expansion of 2.2 mL, which is similar to the volume expansion in experiment 1 (**Figure 4**). This data set suggests that the expanding gas fills nearly the entire pore space as shown in **Figure 5A.** One can, therefore, conclude that the gas was nucleated and almost fully expanded into all available pore space and then re-compressed in two subsequent steps arriving at a non-percolating distribution of gas bubbles as shown in **Figure 8A.** Upon pressure depletion the gas saturation increased again, and gas clusters grew increasing their connectivity (**Figure 8B-D**). Connectivity of the gas in the horizontal direction is already encountered at 2.8 bar (**Figure 8B**) but vertical connectivity is observed only at 2.4 bar displayed in **Figure 8D**.

Fluid Connectivity and Percolation Threshold

The connectivity of the gas phase in experiments 1 and 2 was assessed via the Euler characteristic χ , which is a measure of connectivity and state variable for multiphase flow in porous media [30-32]. For our case the Euler characteristic for the gas phase can be defined as [30]

$$\chi = objects - loops \qquad \text{eq. 1}$$

The Euler characteristic is directly computed on the segmented image using Avizo [32]. Note that χ=0 is an indication for the percolation threshold and is therefore a convenient measure to determine the critical gas saturation S_{gc}. The Euler characteristic as a function of gas saturation is displayed in **Figure 9**, indicating that S_{gc}=0.25 for the pressurization mode and S_{gc}=0.2 for the pressure depletion mode. That is consistent with the range of typical percolation thresholds of 3D structures as listed in Table 1.

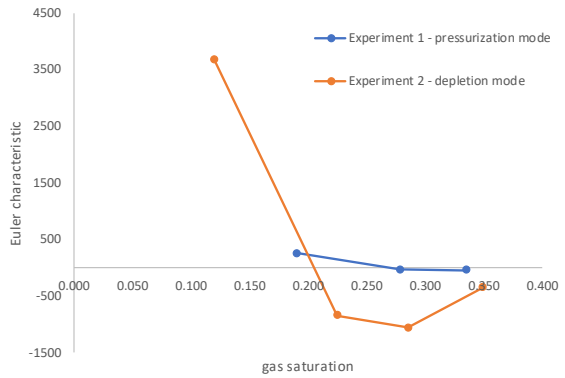

Figure 9. Euler characteristic as a function of gas saturation for experiments 1 and 2. The zero-crossing of the Euler characteristic indicates the percolation threshold, which is around S_{gc}=0.25 for the pressurization mode and S_{gc}=0.2 for the pressure depletion mode.

The difference in critical gas saturation in pressurization and depletion mode ultimately reflects that re-pressurisation is not simply the reverse of primary depletion, as the previously developed phase does not simply retract from the latest pores invaded during depressurization. Rather, the process exhibits a large degree of hysteresis in both local super saturation and gas phase distribution [10].

Table 1. Percolation Threshold in 3D

Structure	Coordination number	Percolation threshold	Ref.
Simple cubic lattice	6	**0.30-0.31**	18-23
BCC lattice	8	**0.243-0.246**	18-23
FCC lattice	12	**0.195-0.199**	24
Random sphere pack	6	**0.31**	25

Note that the top-bottom connectivity does not always coincide with the zero crossing of the Euler characteristic. This might be related to the fact that the Euler characteristic is a measure of isotropic connectivity.

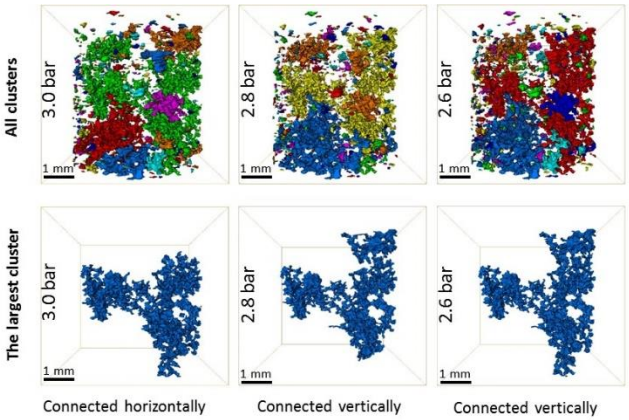

Figure 10. 3D fluid distribution in a pressure depletion experiment (similar to experiment 2) showing all clusters on the top panel and only the largest cluster at the bottom.

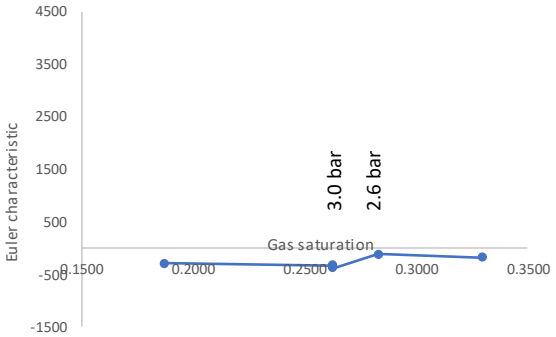

Figure 11. Euler characteristic for the 3D fluid distributions from **Figure 10** plotted at the same scale as in **Figure 9**.

In **Figure 10** the 3D fluid distribution in a pressure depletion experiment (similar to experiment 2) is displayed showing all clusters on the top panel and only

the largest cluster at the bottom. The respective Euler characteristic χ is shown in **Figure 11**. At 3.0 bar the largest cluster percolates horizontally, but not vertically. The Euler characteristic values shown in **Figure 11** are all negative, indicating connectivity, which is aligned with the visual inspection of the identified gas clusters.

Relative Permeability

Apart from the critical gas saturation, the associated relative permeability of gas and liquid are the key parameters of interest [6-7,40]. Traditionally, relative permeability is determined by flow experiments. However, in practical situations the applied pressure gradients and associated viscous instabilities would likely impact the fluid distribution which results in large uncertainties in the determination of relative permeability via flow experiments. Instead, here the 3D spatial distribution of liquid and gas phases from the segmented micro-CT scans were used to compute (connected pathway) relative permeability following a similar methodology as in [36] using a multi-relaxation time lattice Boltzmann method running on distributed GPU [35]. That is possible because the flow regime of connected pathway flow dominates, and -at least in water-wet rock- the flux contribution of ganglion dynamics is expected to be small [37,38].

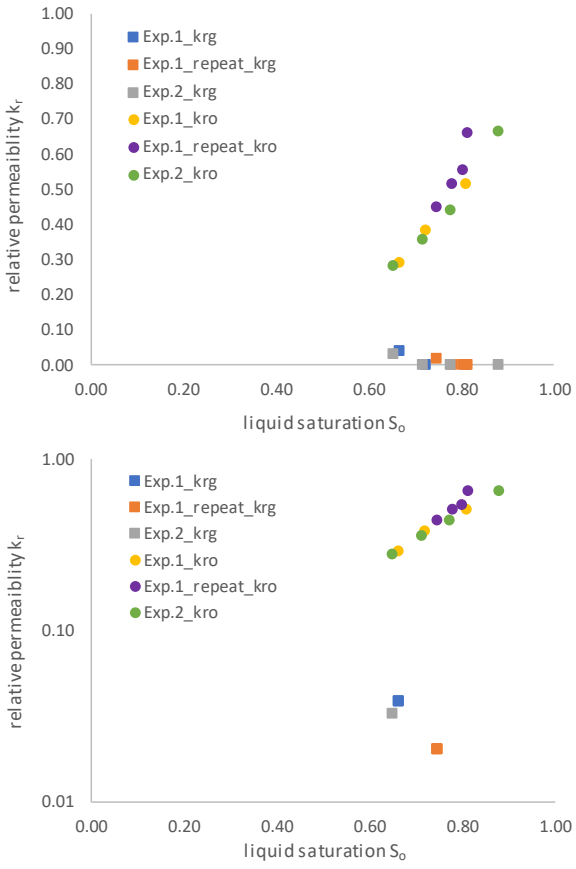

Figure 12. Relative permeability for liquid ("oil", o) and gas (g) computed with a single-phase multi-relaxation time lattice Boltzmann code based on the 3D fluid distribution from the experiments measured by micro-CT on a linear (top) and logarithmic scale (bottom).

The results are displayed in **Figure 12** on a linear (top) and logarithmic scale (bottom). The relative permeability curves are not straight lines as in a near-miscible situation [40]. That is consistent with a interfacial tension of approximately 17 mN/m derived from the PVT EOS calculations. The simulated relative permeability curves appear to be more compatible with a typical Corey behaviour [28] with exponents n_w>1 and n_o>1. The relative permeabilities of experiment 1 and a repeat experiment both conducted in pressurization mode, as well as experiments 2 carried out in pressure depletion mode overlap within the experimental uncertainty. That is somewhat surprising because the pressurization mode is in the widest sense an imbibition process while the pressure depletion is in the widest sense a drainage process, and hysteresis is expected. However, the saturation range is too narrow to clearly identify hysteresis. The fact that no hysteresis was observed could also be explained by the nature of the pores affected. In this case we remain at high gas saturation within or around the percolation threshold and it is likely that hysteresis here could play a minor role.

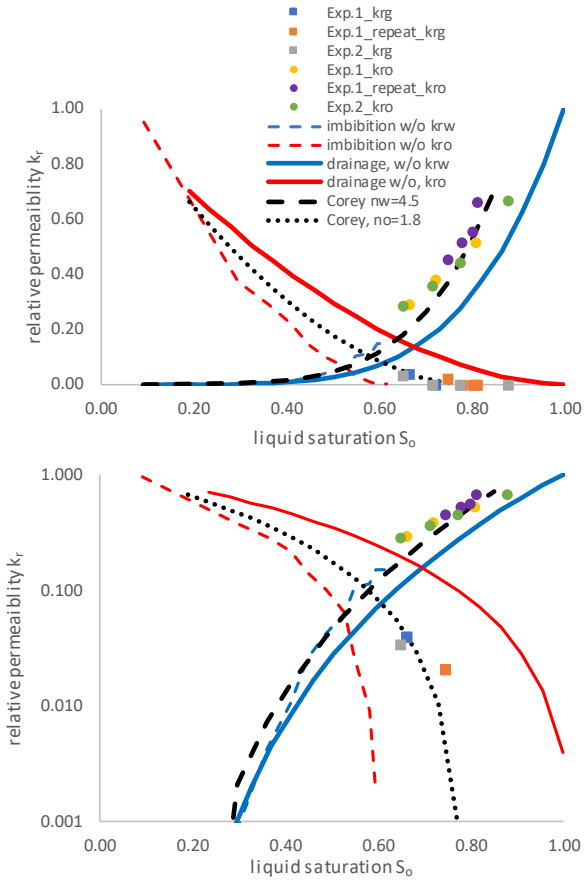

Figure 13. Gas-liquid relative permeability from **Figure 12** on a linear (top) and logarithmic scale (bottom). For comparison, wetting and non-wetting phase relative permeability for water-oil (w/o) are added, both in drainage and imbibition mode (solid and dashed red and blue lines). The gas relative permeability falls right between drainage and imbibition data. The liquid relative permeability seems to follow an extension of the water-relative permeability (dashed black line).

We observe $k_{r,g}>0$ only for Euler characteristic $\chi<0$ which supports the view that the Euler characteristic χ is a meaningful measure for the critical gas saturation. The dynamic range covered in these experiments was not sufficient to establish a $k_{r,g}(\chi)$ relationship as in [33]. In **Figure 13** water-wet water-displacing-oil drainage and imbibition relative permeabilities from a steady-state special core analysis measurement were added for comparison. The measurements were conducted on a 1.5" twin sample using brine-decalin on water-wet (cleaned) rock. The drainage data is shown as solid red and blue lines, the imbibition data is shown as dashed lines. In that comparison the water relative permeability is the wetting phase and oil is the non-wetting phase. In the gas-out-of-solution micro-CT experiment, oil is the wetting phase (because in absence of water it is a liquid and therefore the wetting phase) while gas is the non-wetting phase. Hence, we should compare the gas-out-of-solution liquid relative permeability with the water/oil relative permeability, and gas with oil, respectively. One would expect the liquid relative permeability to follow a primary drainage water line because gas-out-of-solution seems to be associated more with a drainage process. Interestingly the liquid relative permeability does not follow a primary drainage wetting phase relative permeability but rather the same trend as an imbibition relative permeability shown as dashed black line in **Figure 13** (which is an extension of the water imbibition relative permeability using a Corey representation with an exponent n_w=4.5). The gas relative permeability does not seem to follow either a primary drainage or a first imbibition trend. This reflects the fact that gas can come out of solution before a percolation threshold is reached. When comparing with an imbibition data set, this gas saturation would be therefore automatically below the residual oil saturation and hence the relative permeability cannot follow the imbibition line, at least not without re-normalizing the mobile saturation range. A primary drainage oil relative permeability would not be compatible because in primary drainage the non-wetting phase becomes mobile immediately while in the gas-out-of-solution study mobile gas is only possible from the critical gas saturation on. Therefore, the critical gas saturation of $S_{o,crit}$=0.21 is a logical value for a irreducible non-wetting phase saturation. And indeed, when using this re-normalization of the mobile saturation range the gas relative permeability is consistent with a drainage relative permeability as shown in the dotted black line in **Figure 13** (using $S_{or}=S_{o,crit}$=0.21 and n_o=1.8 which is consistent with both drainage and imbibition oil k_r). The liquid relative permeability could also just be a matter of re-scaling to the right end-point saturation, but it is not S_{gc}.

Injection mode

The experiments shown so far were all conducted in absence of external flow addressing the expected slow depletion deep in the reservoir. There is certainly some flow because of expansion (or compression) of gas, but no external gas injection or flow via a pressure gradient was applied. In order to address the scenario near the wellbore, i.e. where gas flows in a potentially unstable fashion, a series of experiments were conducted where pure propane was injected into the propane-decane mixture. The first experiment was conducted at a pressure below the calculated bubble point but above the bubble point observed in previous experiments.

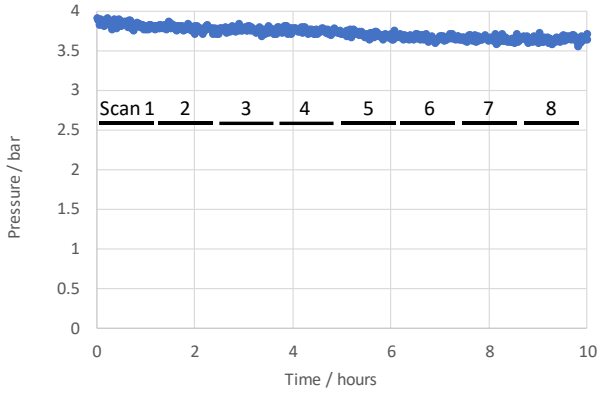

Figure 14. Pressure during flow at low Pe. At nearly constant pressure propane is injected into the Bentheimer core at constant rate of 0.03 ml/h. Respective micro-CT scan intervals are indicated as black lines.

The pressure data of experiment 3 and respective scan intervals are shown in **Figure 14**. Scans were taken continuously where the first scan was taken right after injection started but before gas entered the rock. Propane was injected into the ~50:50 propane-decane mixture at a rate of 0.03 ml/hour. That translates into a Darcy velocity of 2.39 mm/h and a capillary number of $Ca=6\cdot10^{-8}$ (for a liquid viscosity of 0.296 mPa s, calculated from the EOS). The 3D distribution of gas (and respective cluster analysis) is shown in **Figure 15**. Even though there is no visible connectivity from top-to-bottom, already at the first scan there is disconnected gas present in the whole sample. All values of the Euler characteristic χ are near-zero as shown in **Figure 16** indicating a near-percolating situation.

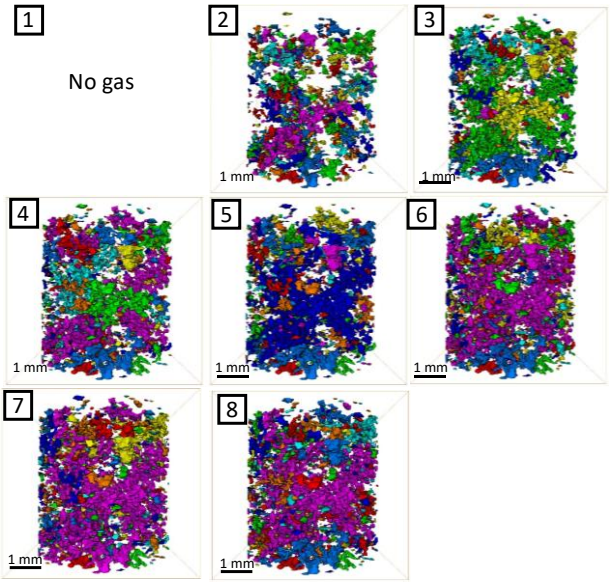

Figure 15. 3D visualization of the gas phase during the constant rate propane injection for the scan intervals from **Figure 14**. From scan 6 on there is top-bottom connectivity.

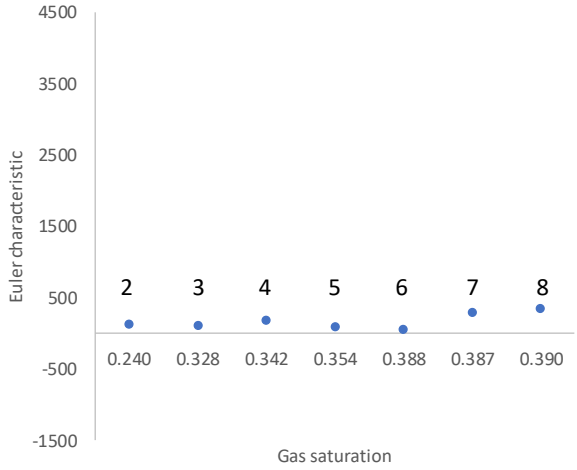

Figure 16. Euler characteristic χ for the 3D gas distribution from **Figure 15**. $\chi>0$ indicating a lesser degree of connectivity.

Actual top-to-bottom connectivity was observed from scan 6 onwards. One the one hand we have to keep in mind that permanent connectivity is not a necessary pre-requisite for flow. Processes such as snap-off in drainage [41] have been observed both experimentally [42] and in direct numerical calculation [43]. Cooperative dynamics such as ganglion dynamics [44] can lead to saturation distributions without permanent connectivity or connected pathway flow to inlet or outlet. Such a situation has been observed in previous synchrotron-beamline based studies with significantly higher time resolution (see Fig. 4 in [42]). Even at a few seconds time resolution the relatively fast snap-off processes which last only few milliseconds were not resolved. With the very limited time resolution of benchtop-based µCT it is difficult fully reveal the microscopic displacement mechanisms. Only a significantly higher time resolution would be able to resolve the exact processes leading to the gas distributions in **Figure 15** before a permanent top-bottom connectivity has been established.

What is striking is that an extended 3D spatial distribution is not only observed in scan 1 but also in the subsequent scans including up to scan 5. Permanent top-bottom connectivity is only observed form scan 6 on. That degree of saturation changes in 3D without permanent connectivity is beyond of what has been observed in simple drainage experiments where only occasionally a connection through a single pore throat was missing [42]. Therefore, the question arises whether there are additional mechanisms at play. One possible hypothesis is that during injection of propane the composition changes locally to a higher propane concentration which would lead to an increase in the bubble point. Therefore, even at a pressure above the bubble point experimentally observed in the previous constant-rate depletion experiments, the pressure would be below the local bubble point which could lead to an unstable growth and propagation of gas bubbles. This mechanism is possible because the Péclet number $Pe=L\cdot v/D\sim 4\cdot 10^{-2}$ for a characteristic length scale $L\sim 60$ µm (typical pore body diameter for Bentheimer sandstone), a typical molecular self-diffusion coefficient for hydrocarbon mixtures of $D\sim 5.8\cdot 10^{-9}$ m^2/s [45] and an interstitial flow velocity of $v\sim 3.5$ µm/s. With Pe much smaller than one the diffusive processes dominate over convection which means that propane could indeed diffuse into the liquid (faster than the flow) and increase the local propane concentration substantially. For the given diffusion coefficient, diffusion across a 60 µm large pore would take about 1 s. To which extent exactly the local composition really changes and how much that really leads to an increase in local bubble point pressure is difficult to estimate without a detailed computation of transport and mass transfer which is beyond the scope of this work.

However, at a higher injection rate the flow would be more convection dominated and less diffusion dominated. By increasing the injection rate by a factor of 30 the Péclet number increases to $Pe\sim 1$ which essentially means that the diffusion is only about as fast as the flow. In comparison with the lower flow rate the onset of a more convection dominated regime and the effect of local compositional changes might be less. Therefore, the injection experiment was repeated at a 30 times higher flow rate of 0.9 ml/h which translates into a Darcy velocity of 72 mm/h and respective capillary number of $Ca=1.8\cdot 10^{-6}$. The pressure and micro-CT scan intervals are indicated in **Figure 17**. The respective 3D gas distribution is displayed in **Figure 18**.

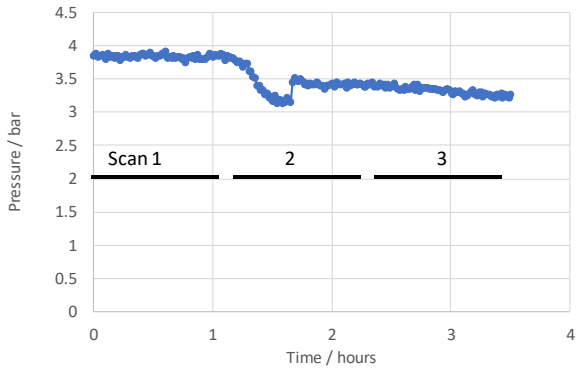

Figure 17. Pressure during experiment 4. Propane is injected into the Bentheimer core at a constant rate of 0.9 ml/h. Respective micro-CT scan intervals are indicated as black lines.

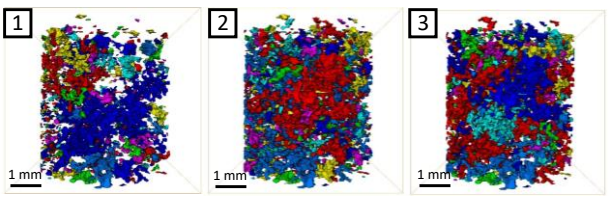

Figure 18. 3D visualization of the gas phase during the constant rate propane injection for the scan intervals from **Figure 17**. Note that in scan 2 and 3, there is permanent top-bottom connectivity.

Note that for the 3D gas distribution displayed in in **Figure 18** scan 2 and 3 have permanent top-to-bottom connectivity and even though no top-bottom connection has been made yet the overall connectivity of scan 1 is already higher than scan 2 or 3 in **Figure 15** (which has

a comparable gas saturation). The connectivity is still higher than even scan 5 in **Figure 15** which is the last scan before permanent top-bottom connectivity was established. Also judging from the Euler characteristic χ displayed in **Figure 19**, which is negative, there is an overall higher degree of connectedness than in the lower flow rate injection experiment from **Figure 16**, i.e. less gas distribution without obvious connectivity to inlet.

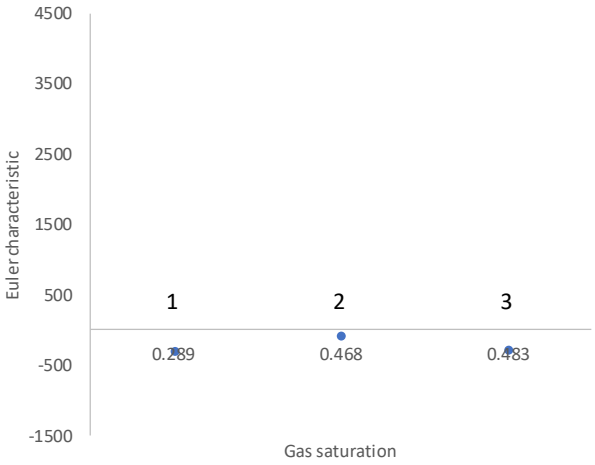

Figure 19. Euler characteristic χ for the 3D gas distribution from **Figure 18**. χ<0 indicating a higher degree of connectivity.

The robust conclusion is that the two injection experiments conceptually differ in terms of fluid connectivity. The increase in flow rate by a factor of 30 does not change the flow regime in terms of capillary number ($Ca=6\cdot10^{-8}$ and $Ca=1.8\cdot10^{-6}$ are both still in the capillary dominated regime) but does change the regime in terms of Péclet number (from $Pe<<1$ to $Pe\sim1$). The more convection dominated regime has the higher degree of permanent connectivity. That supports to some extent the hypothesis of the unstable character of gas injection based on local compositional changes at the $Pe<<1$ case. Potentially the $Pe<<1$ process could also contribute to some observation classically made during tertiary gas injection (below miscibility) with the formation of an oil bank ahead the gas breakthrough. Injecting gas at higher pressure than the bubble pressure could lead, in addition to the standard swelling to sweeping the pore space. Further investigations and modelling work could help to further elucidate the phenomenon.

Relative Permeability

In **Figure 20** the Gas-liquid relative permeability data from the flow experiments were super-imposed on the pressurization and depletion experiments without flow. While the liquid relative permeability is following closely the trend of the pressurization/depletion experiments, the gas relative permeability is clearly different, which could be caused by the fact that the gas is mobile without a permanent connectivity.

When plotting in **Figure 21** all gas relative permeability data vs. Euler characteristic χ there are two distinct populations: All pressure depletion and also high-rate injection experiments show χ<0 as expected for a highly connected phase, whereas for the low rate injection (and presumably diffusion dominated case) χ>0 Indicating a less connected situation.

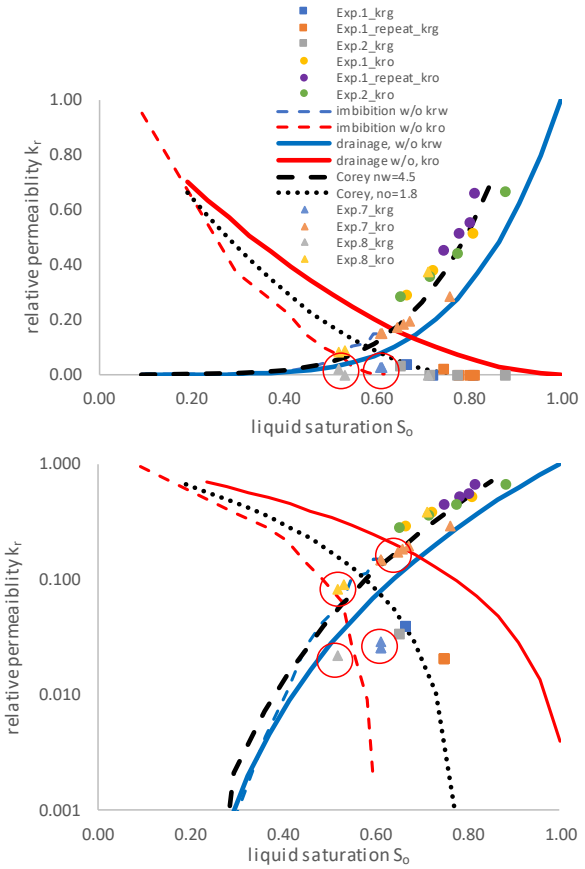

Figure 20. Gas-liquid relative permeability from the flow experiments super-imposed on the pressurization and depletion experiments without flow from **Figure 13**.

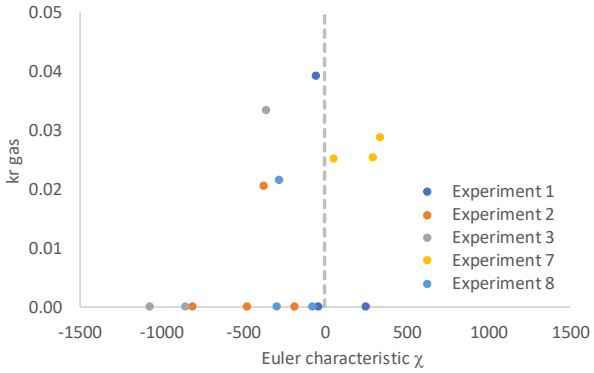

Figure 21. Gas relative permeability vs. Euler characteristic χ. For all pressure depletion (exp. 1-3) and high rate injection experiments (exp 8) χ<0 indicating a connected gas phase. Only for the low rate gas injection case (exp. 7) which is presumably diffusion dominated, χ>0 indicating a non-connected gas phase.

SUMMARY AND CONCLUSIONS

The critical gas saturation has been assessed experimentally via a series of micro-CT flow experiments on a hydrocarbon model system where a gas phase drops

out of solution upon pressure depletion. Pressure depletion in absence of flow provides a proof-of-concept that such critical gas experiments can be indeed conducted via pore scale experimentation. The pore scale distribution of gas was directly imaged by μCT. Consistent with the body of literature, in the porous medium the observation of the bubble point is depressed. The consequence is that nucleation eventually occurs and due to the associated supersaturation [3] the volume of gas dropping out of solution leads to instantaneous percolation, thereby masking the onset of connectivity, i.e. the critical gas saturation. That is an artefact of the experiment conducted at much faster pressure decline rates than the reservoir in the field case [1]. To accommodate for this effect, two protocols were developed where the first protocol operates in pressurization mode (somewhat similar to an imbibition type of experiment) and in the second protocol gas bubbles were first nucleated by rapid pressure drawdown and then re-pressurization to the bubble point followed by subsequent pressure decline (somewhat similar to a drainage process). The observed critical gas saturations were in the range of known percolation thresholds of 3D structures like random sphere packs. Pressurization and pressure depletion led to noticeably different critical gas saturations which might be related to the underlying difference in pore scale displacement events between drainage and imbibition processes [39]. A so far unresolved question is how the fast depletion – re-pressurization affects the depletion mode experiments.

Respective relative permeability curves were computed from the 3D gas and liquid distributions imaged by micro-CT using an in-house developed multi-relaxation time lattice Boltzmann method. They were then compared with drainage and imbibition water/oil relative permeability from steady-state SCAL data conducted on a (water-wet) twin sample. In that comparison the liquid relative permeability is consistent with an extension of the (wetting) water relative permeability from a water-oil imbibition experiment. The gas relative permeability is not compatible with either a drainage or an imbibition oil relative permeability from SCAL. The main reason is that a critical gas saturation is required before gas becomes mobile, i.e. a relative permeability can be defined. Therefore, the mobile gas saturation range starts at critical gas saturation which is larger than zero (hence the gas relative permeability cannot be compatible with a primary drainage curve) and smaller than a typical residual oil saturation (hence not compatible with a first imbibition relative permeability). However, rescaling the oil primary drainage relative permeability to the mobile saturation range for the gas case using the measured percolation threshold $S_{o,crit}$=0.21 as saturation endpoint does provide good consistency with the gas relative permeability.

The methodology of imaging the gas distribution in a flow experiment was extended to different flow regimes. Injecting gas at a low flow rate led to a 3D gas distribution without any obvious permanent connectivity to the inlet and a positive Euler characteristic $\chi>0$, i.e. below the percolation threshold. In direct comparison, at high injection rate, the connectivity at similar saturations was higher with $\chi<0$, i.e. above the percolation threshold. This could indicate a potentially unstable displacement scenario for the low injection rate case. While the low and the high injection rate experiments fall both within the same flow regime in terms of capillary number, they differ in terms of Péclet number *Pe*. For the low injection rate $Pe<<1$ meaning a much more diffusion-dominated regime, where the gas injected above the bulk liquid bubble point pressure can dissolve into the liquid phase at the injection front and change the respective composition such that the bubble point pressure increases. That can lead to a potentially unstable flow regime, where displacement scenarios become thinkable that do not require permanent connectivity. At the high injection rate, $Pe\sim1$ a higher degree of connectivity above the percolation threshold was observed which is more representative for a typical drainage type of displacement scenario. Note here the self-diffusion coefficient has been used to estimate the diffusive flux. Mutual diffusion coefficients in concentration gradients can be substantially higher which would increase the diffusive flux.

In order to develop the concept for quantifying critical gas saturation using pore scale imaging further, more detailed injection studies need to be conducted at different regimes e.g. in the supersaturated range below the observed bubble point but before gas can nucleate, at an even lower injection rate, and at faster time resolution to identify movement of discontinuous gas clusters. The underlying assumption of most of the current work is the steady movement of a continuous, sample spanning, gas phase at critical gas saturation. That assumption is widely accepted but may not fully cover all possible flow regimes such as gas clusters moving as a discontinuous phase [14-15] somewhat similar to the ganglion dynamics phenomena in immiscible 2-phase flow [37,38]. Relatively high interfacial tension of the chosen model system and the short core would likely suppress the movement of gas clusters. In order to study dynamic phenomena, the fast acquisition of a synchrotron beamline based μCT facility would be required. In low interfacial tension system, at increased time resolution intermittent gas production during gas depletion experiments on cores before the period of sharp gas-oil-ratio increase could be observed.

Our experiments have demonstrated that the hybrid methodology of pore scale experimentation and pore scale modelling provides a useful approach to address complex special core analysis problems that are difficult to achieve or even inaccessible for traditional special core analysis experimentation.

Acknowledgements: Arjen Cense, Keith Love and Birol Dindoruk are acknowledged for helpful discussions that guided the experiments. Willem-Bart Bartels and Hassan Mahani are acknowledged for designing and testing the micro-CT flow cell. Gerald Hamon and Patrick Egermann are gratefully acknowledged for the constructive comments during the review.

References

1. SCHERPENISSE, W., WIT, K., ZWEERS, A.E., SNOEI, G., AND VAN WOLFSWINKEL, A., "Predicting Gas Saturation Build-up During Depressurisation of a North Sea Oil Reservoir". Presented to the SPE Europec Meeting, London, Oct. 1994. SPE 28842 (1994).
2. LIGTHELM, D.J., REIJNEN, G.C.A.M., WIT, K., WEISENBORN, A.J., SCHERPENISSE, W., Critical Gas Saturation During Depressurisation and its Importance in the Brent Field, 1997 Offshore Europe Conference held in Aberdeen, Scotland, 9-12 September 1997, SPE-38475 (1997).
3. FIROOZABADI, A., OTTESEN, B., MIKKLESEN, M., Measurements and Modelling of Supersaturation and Critical Gas Saturation, SPE 19694, San Antonio, October 1989.
4. KAMATH, J., BOYER, R.E., Critical Gas Saturation and Supersaturation in Low-Permeability Rocks, SPE 26663, SPE Formation Evaluation, 247-253, December 1995.
5. DU, C., YORTSOS, Y. C., A Numerical Study of the Critical Gas Saturation in a Porous Medium, Trans. Porous Med. 35, 205-225 (1999).
6. EGERMANN, P., VIZIKA, O., Critical Gas Saturation and Relative Permeabilty During Depressurization in the Far Field and the Near-Wellbore Region, 2000 SPE Annual Technical Conference and Exhibition held in Dallas, Texas, 1-October 2000, SPE-63149 (2000)
7. EGERMANN, P., VIZIKA, O., A New Method to Determine Critical Gas Saturation and Relative Permeability During Depressurization in the Near-wellbore Region, Petrophysics 42(4), 352-361 (2001).
8. PICCAVET, N., LONG, J., HAMON, G., BONDINO, I. MCDOUGALL, S.R., Depletion of Near-Critical Oils : Comparison between Pore Network Model Predictions and Experimental Results, International Symposium of the Society of Core Analysts held in Trondheim, Norway, 12-16 September 2006, SCA2006-32 (2006).
9. BONDINO, I., MCDOUGALL, S.R., HAMON, G., Pore network modelling of heavy oil depressurisation: a parametric study of factors affecting critical gas saturation and 3-phase relative permeabilities, SPE Journal 196-205 (2005), SPE-78976.
10. BONDINO, I., MCDOUGALL, SR., EZEUKO, CC., HAMON, G., Pore-Scale Simulation of Hysteresis Effects During Repressurization of Gas-Oil Systems, SPE Annual Technical Conference and Exhibition held in Florence, Italy, 19-22 September 2010. SPE-134525.
11. GRATTONI, C.A., HAWES, R.I., DAWE, R.A., Relative Permeabilities for the Production of Solution gas from Watereflood Residual Oil, 1998 Annual Symposium of the Society of Core Analysts, SCA-9817 (1998).
12. PETERSEN JR, E.B., AGAEV, G.S., PALATNIK, B., RINGEN, J.K., ØREN, P.E., VATNE, K.O., Determination of Critical Gas Saturation and Relative Permeabilties Relevant to the Depressurization of the Statfjord Field, International Symposium of the Society of Core Analysts held in Abu Dhabi, UAE, 5-9 October, 2004, SCA2004-33 (2004).
13. JI, W., DAHMANI, A., AHLFELD, DP., LIN, JD., HILL, E. III, Laboratory study of air sparging: air flow visualization, Groundwaetr Monitoring & Remediation 13(4), 115-126, 1993.
14. PLUMMER, CR., NELSON, JD., ZUMWALT, GS., Horizontal and vertical well comparison for in-situ air sparging. Ground Water Monitoring Review 17(1), 91-96, 1997.
15. MUMFORD, KG., Spontaneous expansion and mobilization of gas above DNAPL, PhD Thesis, McMaster University, 2008.
16. BULL, O., BRATTELI, F., RINGEN, JK., MELHUUS, K., BYE, AL., IVERSEN, JE., The Quest for the True Residual Gas Saturation - An Experimental Approach, International Symposium of the Society of Core Analysts held in Austin, Texas, USA, 18-21 September, 2011, SCA2011-03 (2011).
17. CENSE, A., REED, J., EGERMANN, P., SCAL for Gas Rservoirs : A Contribution for Better Experiments, International Symposium of the Society of Core Analysts held in Snowmass, Colorado, USA, 21-26 August 2016. Paper SCA2016-023.
18. KIM, T.W., KOVSCEK, A.R., The Effect of Voidage-Displacement Ratio on Critical Gas Saturation, SPE Journal 24(01), 178-199 (2019).
19. SATIK, C., ROBERTSON, C., KALPACKI, B., GUPTA, D. , "A Study of Heavy Oil Solution Gas Drive for Hamaca Field": Depletion Studies and Interpretations", SPE paper 86967 presented at the SPE International Thermal Operations and Heavy Oil Symposium and Western Regional Meeting, Bakersfield, CA, 16-18, March (2004).
20. SAHNI, A., GADELLE, F., KUMAR, M., TOMUTSA, L., KOVSCEK, A., "Experiments and Analysis of Heavy Oil Solution Gas Drive", SPE Reservoir Evaluation & Engineering, pp 217-229, June (2004).
21. XU, X., WANG, J. LV, J.-P., DENG, Y., Simultaneous analysis of three-dimensional percolation models, Frontiers of Physics 9(1), 113-119 (2014).
22. JAN, N., STAUFFER, D., Random Site Percolation in Three Dimensions, International Journal of Modern Physics C 09(02), 341-147 (1998).
23. SYKES, M.F., ESSAM, J.W., Critical percolation probabilities by series method, Physical Review 133(1A), A310-A315 (1964).

24. VAN DER MARCK, S.C., Calculation of Percolation Thresholds in High Dimensions for FCC, BCC and Diamond Lattices, International Journal of Modern Physics C, 9(4), 529-540 (1998).
25. POWELL, M.J., Site Percolation in Randomly Packed Spheres, Physical Review B 20(10), 4194-4198 (1979).
26. VAN WAGENINGEN, W.F.C., MAAS, J.G., Reservoir Simulation and Interpretation of the RECOPOL ECMB Pilot in Poland, 2007 International Coalbed Methane Symposium, Paper 072 (2007).
27. LENORMAND, R., TOUBOUL, E., ZARCONE, C., Numerical models and experiments on immiscible displacements in porous media, J. Fluid Mecha. 189, 165-187 (1988).
28. BERG, S., OEDAI, S., LANDMAN, A.J., BRUSSEE, N., BOELE, M., VALDEZ, R., VAN GELDER, K., Miscible displacement of oils by carbon disulfide in porous media: Experiments and analysis, Physics of Fluids 22, 113102 (2010).
29. BERG, S., OTT, H., Stability of CO2-Brine Immiscible Displacement, International Journal of Greenhouse Gas Control 11, 188-203 (2012).
30. HERRING, A.L., ANDERSSON, L., SCHLÜTER, S., SHEPPARD, A., WILDENSCHILD, D.: Efficiently engineering pore-scale processes: the role of force dominance and topology during nonwetting phase trapping in porous media. Adv. Water Resour. 79, 91 (2015)
31. MCCLURE, J.E., ARMSTRONG, R.T., BERRILL, M.A., SCHLÜTER, S., BERG, S., GRAY, W.G., MILLER, C.T., A geometric state function for two-fluid flow in porous media, Phys. Rev. Fluids 3(8), 084306, 2018.
32. ARMSTRONG, R.T., MCCLURE, J.E., ROBINS, V., LIU, Z., ARNS, C.H., SCHLÜTER, S., BERG, S., Porous Media Characterization Using Minkowski Functionals: Theories, Applications and Future Directions, Transport in Porous Media, 2018 in press doi:10.1007/s11242-018-1201-4
33. LIU, Z., HERRING, A., SHEPPARD, A., ARNS, C., BERG, S., ARMSTRONG, R.T., Morphological characterization of two-phase flow using X-ray microcomputed tomography flow-experiments, Transport in Porous Media 118(1), 99-117, 2017.
34. BUADES, A., COLL, B., MOREL, J.-M., A Non-Local Algorithm for Image Denoising, 2005 IEEE Computer Society Conference on Computer Vision and Pattern Recognition (CVPR'05) 2, 60-65 (2005).
35. ALPAK, F.O., GRAY, F., SAXENA, N., DIETDERICH, J., HOFMANN, R., BERG, S., A Distributed Parallel Multiple-Relaxation-Time Lattice Boltzmann Method on Graphic Processing Units for the Rapid and Scalable Computation of Absolute Permeability from High-Resolution 3D Micro-CT Images, Computational Geosciences 22(3), 815–832 (2018).
36. BERG, S., RÜCKER, M., OTT, H., GEORGIADIS, A., VAN DER LINDE, H., ENZMANN, F., KERSTEN, M., ARMSTRONG, R.T., DE WITH, S., BECKER, J., WIEGMANN, A., Connected Pathway Relative Permeability from Pore Scale Imaging of Imbibition, Advances in Water Resources 90, 24-35, 2016.
37. ZOU, S., ARMSTRONG, R.T., ARNS, J.Y., ARNS, C.H., HUSSAIN, F., Experimental and Theoretical Evidence for Increased Ganglion Dynamics During Fractional Flow in Mixed-Wet Porous Media, Water Resources Research 54 (5), 3277-3289, 2018.
38. ARMSTRONG, R.T., MCCLURE, J.E., BERRILL, M.A., RÜCKER, M., SCHLÜTER, S., BERG, S., Beyond Darcy's law: The Role of Phase Topology and Ganglion Dynamics for Two Fluid Flow, Physical Review E 94, 043113 (2016).
39. SCHLÜTER, S., BERG, S., RÜCKER, M., ARMSTRONG, RT., VOGEL, H.-J., HILFER, R., WILDENSCHILD, D., Pore scale displacement mechanisms as a source of hysteresis for two-phase flow in porous media, Water Resources Research 52(3), 2194-2205, 2016.
40. ALZAYER, A., VOSKOV, D.V., TCHELEPI, H.A., Relative Permeability of Near-Miscible Fluids in Compositional Simulators, Trans. Porous Med. 122(3), 547-573 (2018).
41. ROOF, J.G., Snap-off of oil droplets in water-wet pores. SPE J 10(1):85–90 (1970).
42. BERG, S. ARMSTRONG, R.T., OTT, H., GEORGIADIS, A., KLAPP, S., A., SCHWING, A., NEITELER, R., BRUSSEE, N., MAKURAT, A., LEU, L., ENZMANN, F., SCHWARZ, J.-O., WOLF, M., KHAN, F., KERSTEN, M., IRVINE, S., STAMPANONI, Multiphase flow in porous rock imaged under dynamic flow conditions with fast X-ray computed microtomography, Petrophysics 55 (4), 304-312, 2014.
43. EVSEEV, N., ARMSTRONG, R.T., BERG, S., DINARIEV, O., KLEMIN, D., KOROTEEV, D., SAFONOV, S., Modeling of pore-scale two-phase flow phenomena using density functional hydrodynamics, Transport in Porous media 112(3), 577-607, 2016.
44. RÜCKER, M., BERG, S., ARMSTRONG, R.T., GEORGIADIS, A., OTT, H. SCHWING, A., NEITELER, R., BRUSSEE, N., MAKURAT, A., LEU, L., WOLF, M., KHAN, F., ENZMANN, F., KERSTEN, M., From Connected Pathway Flow to Ganglion Dynamics, Geophysical Research Letters 42, 3888-3894, 2015.
45. REAMER, H.H., OPFELL, J.B., SAGE, B.H., Diffusion Coefficients in Hydrocarbon Systems, Methane-Decane-Methane in Liquid Phase, Ind. Eng. Chem. 48(2), pp 275–282, 1956.